On the emergence of fault afterslip during laboratory seismic cycles

Corentin Noël[1],

↨

Cédric Twardzik[1],

↨

Pierre Dublanchet[2],

↨

François Passelègue[1]

1: Université Côte d'Azur, CNRS, Observatoire de la Côte d'Azur, IRD, Géoazur, Valbonne, France

2: Mines Paris, PSL University, Center for geosciences and geoengineering, Fontainebleau, France

Corresponding author: Corentin Noël (corentin.noel@geoazur.unice.fr)

Highlights:

- Triaxial deformation of frictionally heterogeneous faults
- Co-seismic events of frictionally heterogeneous faults are followed by afterslip
- Afterslip magnitude depends on the frictional properties and on the normal stress acting on the fault

Abstract

Spatial fault heterogeneity is often invoked to explain the occurrence of fault afterslip following seismic ruptures. In this study, we tested this hypothesis in the laboratory by performing triaxial experiments on both homogeneous and heterogeneous faults, under confining pressures of 30, 60, and 90 MPa. The faults were composed of granite, prone to seismic behaviour, and marble, prone to aseismic behaviour. Unlike homogeneous granite faults, which display a nucleation stage followed by regular seismic events, heterogeneous faults can contain the co-seismic dynamic event within the experimental fault length. During this phase, the aseismic areas adjacent to the dynamic event undergo a stress increase, which is then released by fault afterslip over an extended post-seismic phase. The magnitude and duration of this post-seismic phase increase with confining pressure and with the proportion of aseismic areas. We infer that the enhancement of post-seismic afterslip originates from the increase in the frictional stability of the aseismic area, and of the normal stress acting on the fault. In addition, the observed increase in initial strain rate with normal stress is well explain by the rate-and-state framework. At the scale of our experiments, fault frictional heterogeneities play a primary role in the emergence of fault afterslip.

Keywords: Fault heterogeneity, seismic cycle, post-seismic deformation, afterslip.

1. Introduction

Recent geodetical and seismological observations have revealed that a significant proportion of earthquakes exhibit prolonged fault afterslip, primarily characterized by aseismic fault movement in the surrounding of the seismically ruptured zone (e.g., Barbot et al., 2009; Cheloni et al., 2010; Smith & Wyss, 1968; Yagi et al., 2001, 2003. See Avouac (2015) for an extensive review). Importantly, the moment released by fault afterslip can be as large as, or even larger than the co-seismic moment (Barbot et al., 2009). Because of that, fault afterslip is expected to contribute significantly to the energy release along the fault during the seismic cycle, as well as to stress transfer in areas devoid of recent seismic rupture.

To understand the physical parameters controlling the emergence of fault afterslip, numerical models have been developed, primarily based on rate-and-state friction laws (Dieterich, 1978; Ruina, 1983). Within this framework, fault afterslip is typically explained by spatial frictional heterogeneities, where velocity-weakening and velocity-strengthening regions interact (Marone et al., 1991; Rice & Gu, 1983). In these models, the co-seismic event is confined to the velocity-weakening zone, which induces stress perturbations and a slip deficit in the velocity-strengthening region, that is subsequently retrieved (at least partially) by aseismic fault afterslip, and often associated with aftershocks (Perfettini & Avouac, 2007). Other models suggest that the presence of stress heterogeneities can induce the emergence of fault afterslip (Helmstetter & Shaw, 2009; Hirose & Hirahara, 2004). In this case, afterslip can occur on a velocity-weakening fault zone presenting a stress level that is too low to trigger earthquakes or to permit the adjacent rupture to propagate through this area. Finally, a recent study suggests that fault afterslip can be generated on any portion of the fault presenting a geometric moment deficit (the product of slip and rupture area) following an earthquake (Meade, 2024). While these models can effectively describe fault afterslip following earthquakes (e.g., Barbot et al., 2009; Fukuda et al., 2009; Gualandi et al., 2017; Helmstetter & Shaw, 2009; Lin et al., 2013; Perfettini et al., 2010; Perfettini & Avouac, 2004, 2007; Wimpenny et al., 2017), assumptions are needed in order to estimate the physical parameters that govern fault afterslip, especially due to the unknown stress conditions.

To understand further the emergence of fault afterslip, laboratory experiments have been conducted along homogeneous and heterogenous fault interfaces. For example, Caniven et al.

(2015) demonstrated that post-seismic deformation (both afterslip and viscoelastic relaxation) can be observed in a strike-slip heterogeneous fault system only, composed of a polyurethane foam placed on a silicone layer, representing the seismic upper crust and the ductile lower crust, respectively. Similarly, in analogue experiment of subduction systems, introducing viscoelastic coupling between the overriding plate and the mantle wedge facilitates the post-seismic viscoelastic relaxation phase (Caniven & Dominguez, 2021). On bare rock interfaces, afterslip has been observed due to pore fluid pressure recharge of the fault following a co-seismic event (Aben & Brantut, 2023). In this scenario, afterslip is co-located with the main rupture zone, contrary to what is typically observed in natural earthquakes. Afterslip has also been observed, though to a limited extent, on large bi-axial faults composed of homogeneous granite interface (Ke et al., 2021). When ruptures are confined, limited afterslip occurs at the rupture arrest tip, releasing about 5% of the stress deficit, which is significantly smaller than what is observed for large earthquakes (Barbot et al., 2009; Cheloni et al., 2010; Smith & Wyss, 1968; Yagi et al., 2001, 2003). To our knowledge, laboratory experiments conducted on bare rock interfaces have not yet reproduced large afterslip similar to what is observed after large natural earthquakes, which is characterized by significant slip amplitude occurring outside of co-seismic slip patch.

Here, we tackle this issue by conducting laboratory triaxial experiments of homogeneous and heterogeneous faults composed of Westerly granite (prone to seismic behaviour) and Carrara marble (prone to aseismic behaviour) (Figure S1). The experiments were performed at confining pressure (P_c) ranging from 30 to 90 MPa to investigate the effect of different depth on heterogeneous fault's seismic cycle. These experiments allowed, for the first time, to reproduce afterslip in a triaxial apparatus, and to estimate the parameters controlling the distribution of fault slip during the different stages of the seismic cycle.

2. Experimental methods

Two lithologies were used for the study: Westerly granite (Rhode Island, USA) and Carrara marble (Tuscany, Italy). These lithologies were selected because they are well studied in the literature (Fredrich et al., 1989; Lockner, 1998; Schmid et al., 1980; Tullis & Yund, 1977; Wong, 1982) and have opposite frictional properties. Under the tested conditions, laboratory experiments show that bare surface fault of Westerly granite are prone to seismic behaviour (Lockner et al., 2017; Passelègue et al., 2016; Thompson et al., 2009), related to a velocity weakening behaviour (Dieterich, 1979; Ruina, 1983). On the contrary, in the tested conditions, Carrara marble is prone to aseismic behaviour (Aubry et al., 2020; Carpenter et al., 2016; Verberne et al., 2014), related to velocity-strengthening behaviour, and can experience a brittle-ductile transition at high confining pressure (P_c > 50 MPa (Fredrich et al., 1989; Meyer et al., 2019)).

Five faults, composed of homogeneous and heterogeneous half-sample, were tested: (i) granite-on-granite fault (G_f), (ii) granite-on-granite with a marble asperity (M_{asp}), (iii) granite-on-marble with a granitic asperity (G_{asp}), (iv) granite-on-marble fault (GM_f), and (v) marble-on-marble fault (M_f) (Figure S1). All experiments were conducted in a triaxial loading apparatus developed by CoreLabs (Brantut et al., 2011; Passelègue et al., 2016). Both axial and radial pressure were monitored using pressure transducers (±50-kPa resolution). The axial displacement (d_{ax}) was measured using three external gap sensors having a 0.1-µm resolution. In addition, 8 strain gauges were deployed around the fault (Figure S2), allowing to record local strain measurement during the sample deformation. These strain gauges were glued parallel to the axial stress (σ_{ax}) as close as possible to the fault. Note that the strain gauges were always glued on the granite half sample (except for the M_f), to insure measurement on a homogeneous medium. During the sample deformation, all the mechanical data were recorded at 2400 Hz sampling rate. An experiment consists in two main steps. After placing the fault assemblage into the deformation apparatus, we first conducted successive deformation at 30, 60 and 90 MPa confining pressure. During these three consecutive stages, the roughness of the fault is expected to evolves with the cumulative displacement and with the increase of stress at fault asperities. Because of that, in a second step, we conducted two additional experiments, decreasing first the confining pressure back to 60 MPa, and finally to 30 MPa. In the following, we mainly focus on the experiments conducted during the first step (i.e., successive increase in confining pressure). The results of the experiments conducted during the unloading steps will be discussed in the section 4 only. For additional information on the experimental methods, please refer to the Supplementary Material section 1.

3. Experimental results

3.1. Macroscopic measurements

The experimental results show that the fault slip behaviour depends primarily on the sample composition (Figure 1), and secondarily on the confining pressure. As expected, our two end-members tested fault show opposite seismic behaviour. G_f shows typical repeated stick-slip (i.e., seismic) behaviour with co-seismic shear stress drop ($\Delta\tau$) increasing from ~ 3.3 to 14.8 MPa with increasing P_c from 30 to 90 MPa. In these experiments, most of the slip occurs seismically (Figure 2a), as observed in previous studies (Lockner et al., 2017; Passelègue et al., 2016; Thompson et al., 2009). Conversely, M_f shows stable sliding behaviour for all the tested P_c. The heterogeneous samples (G_{asp}, M_{asp}, and GM_f) all show repeated stick-slip behaviour. Interestingly, the macroscopic stress drop is decreasing with increasing marble content. For example, at P_c = 30 MPa, $\Delta\tau$ is reduced from ~ 1.5 MPa for M_{asp} to 1 MPa for G_{asp}. For all the heterogeneous samples, increasing the confining pressure favour larger macroscopic stress drop (Figure 1).

To analyse further the influence of heterogeneities on the different stages of the seismic cycle, we now describe the evolution of the shear stress and of the fault slip before, during and after the main instabilities. For all the experiments, the inter-seismic phase is characterized by an elastic stage, highlighted by a linear increase in shear stress during which no slip is observed (Figure 2). This phase ends when the shear stress reaches a critical value allowing the initiation of fault slip. At this point, the faults enter in a pre-seismic phase (or nucleation phase), which is characterized by a deviation from linearity in the macroscopic shear stress, and by the onset of fault slip (yellow areas, Figure 2a-d). The amount of slip during this stage remains small, but is systematically observed. Following the nucleation phase, a rapid macroscopic stress drop associated with fault slip is observed (Figure 2a-d). As expected from the values of the stress drop, increasing the content of marble leads to a decrease of the co-seismic slip (Figure 2). For G_f, the amount of co-seismic slip increases from 34 to 116 µm with increasing the confining pressure from 30 to 90 MPa (Figure 2e-g). For the heterogeneous fault (M_{asp}, G_{asp} and GM_f), the amount of co-seismic slip is about 7-15 µm in average at P_c = 30 MPa, and of 13-25 µm at higher confining pressure (Figure 2e-g).

The main result of our study is that following the co-seismic phase, heterogeneous faults exhibit an extended period of slip (Figure 2). This behaviour is particularly well observed for G_{asp} and GM_f, where fault slip continues after the co-seismic phase over a non-negligible amount of time (from 1 to 1.5 second at P_c = 90 MPa, blue areas in Figure 2c and d). Remarkably, in the case of G_f, no fault afterslip is observed. Our results demonstrate that the presence of a single marble asperity (M_{asp}) allows fault afterslip to take up to 10% of the total slip (i.e., pre-, co- and post-seismic slip, Figure 2e-g). Increasing the content of marble tends to enhance fault afterslip. G_{asp} and GM_f show the largest and the longest afterslip stages. For these faults, afterslip represent up to 28% of the total slip. Additionally, the fault afterslip increases with P_c, increasing for example from 17% to 27% with increasing P_c from 30 to 90 MPa for G_{asp} (Figure 2e-g).

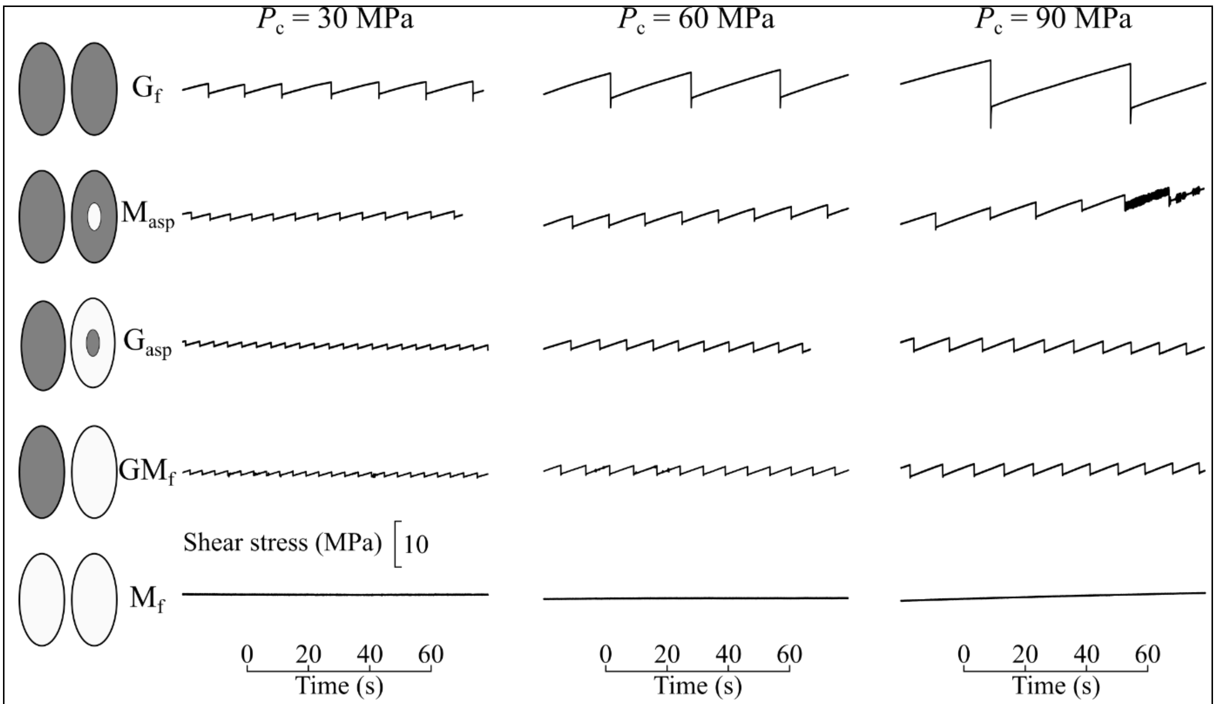

Figure 1: Shear stress as a function of time for the 5 tested fault compositions and three tested confining pressures. The symbols of the left represent the two sides of the fault tested (grey for granite and white for marble). Note that the shear stress and time axes are the same for all the data plotted. For the full mechanical curves see Figure S4 in the supplementary material.

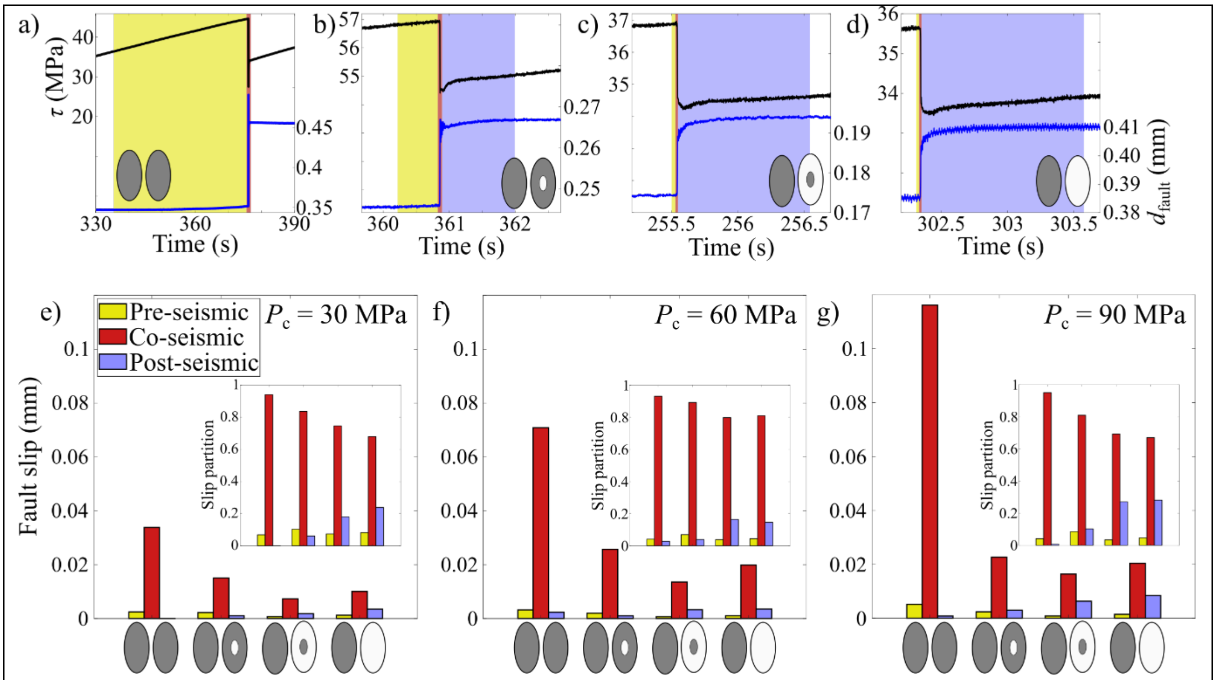

Figure 2: a-d) Shear stress (black curves) and fault displacement (blue curves) as a function of time measured during a typical event at P_c = 90 MPa on a) granite-on-granite (G_f), b) granite-on-granite with marble asperity (M_{asp}), c) granite-on-marble with granite asperity (G_{asp}), and d) granite-on-marble (GM_f) samples. The yellow, red and blue zones represent the pre-seismic, co-seismic and post-seismic phases, respectively. e-g) Fault slip (average of all the events) recorded during pre-seismic, co-seismic and post-seismic phases for the tested fault that experienced seismic behaviour for e) P_c = 30 MPa, f) P_c = 60 MPa and g) P_c = 90 MPa. The symbols of the x-axis represent the two sides of the fault tested (grey for granite and white for marble). In each plot, the insert represents the fault slip distribution for each tested condition.

3.2. Local strain measurements

To analyse the slip distribution during the different stages of the seismic cycle, the array of strain gauges measuring axial strain variation close to the fault was used. In the following the influence of heterogeneity on the nucleation, co-seismic and post-seismic phases are described using this array.

3.2.1 Nucleation of instability

As observed in the macroscopic measurements (Figure 2), the initiation of the nucleation stage is highlighted by the strain gauges array when the inelastic strain (see Supplementary Material section 1.4) departs from 0 (Figure 3 and Figure 4). Note that a decrease in inelastic strain is a proxy for fault slip, while an increase in inelastic strain is a proxy for fault stick (or slipping less than the rest of the fault). The nucleation stage is clearly marked for G_f, where the onset of nucleation, associated with the propagation of a quasi-static slip front, can be tracked spatially. The quasi-static slip front initiates in the upper part of the fault (blue and green curves on Figure 3a-c, Figure 4a, and Figure S7a-c) and propagates toward the bottom of the fault (Figure 3a-c and Figure 4a).

In the case of heterogeneous fault, the nucleation stage is more complicated. For M_{asp}, at confining pressures of 30 and 60 MPa, the initiation of the pre-seismic phase is more localized at the granite-granite contacts (Figure S7d-f). Meanwhile, inelastic strain near the asperity (yellow and green curves in Figure S7d-f) is increasing, indicating that this part of the fault remains locked. However, at P_c = 90 MPa, the nucleation is predominantly confined to the bottom left of the sample (orange curve in Figure 4b), while other parts of the fault remain locked. For G_{asp}, the pre-seismic phase is primarily confined to the bottom of the asperity (orange curve in Figure 3g-i, Figure 4c and Figure S7g-i), while the rest of the fault experiences an increase in strain. Note that for this sample, an aborted pre-seismic phase could also be observed on the top of the asperity (green curve on Figure 4c). Finally, for GM_f, the pre-seismic phase is mainly confined to the bottom of the fault, with the top part remaining locked (Figure 3j-l, Figure 4d and Figure S7j-l). Notably, for all tested fault and confining pressure conditions, the onset of the nucleation phase coincides with the location of maximum recorded stress (Figures S9 and S10), i.e., where the static friction is the highest.

3.2.2 Co-seismic phase

The strain gauges array can be used to track the propagation of the seismic rupture (Passelègue et al., 2020). For G_f, the dynamic strain drop occurs at the same time on all the strain gauges (Figure 3a-c, Figure 4a and Figure S7a-c). Our temporal resolution does not allow us to see any propagation of this strain drop front, which means that the front must propagate at least at 190 m/s, and that the co-seismic rupture propagates through the entire fault.

For M_{asp}, the dynamic strain drop also occurs on all the strain gauges at the same time, indicating fast rupture velocity. Additionally, at P_c = 90 MPa, the two strain gauges located at the top of the sample measure an increase in strain rather than a drop (Figure 4b) suggesting that this part of the fault did not break co-seismically. In the case of G_{asp}, a rapid strain drop is observed only on the strain gauges located close to the asperity (i.e., at the centre of the fault, Figure 4c). Strain gauges located further from the asperity experience a large increase in strain. Finally, for GM_f, the co-seismic strain drop is also confined close to the nucleation zone (orange curves on Figure 3j-l and Figure 4d). For G_{asp} and GM_f, increasing the confining pressure favour a smaller spatial extent of the co-seismic rupture (Figure S7j-l).

3.2.3 Afterslip phase

The strain gauges array also recorded the signal of fault afterslip during the post-seismic stage. For the heterogeneous samples (particularly for the ones with high marble content), after the co-seismic phase, some strain gauges show a long strain release (Figure 3, Figure 4 and Figure S7). This long strain release is located in areas devoid of co-seismic strain drop, i.e., where a strain deficit has accumulated during the co-seismic phase.

For G_{asp}, the strain gauges located far from the seismic asperity exhibit a large increase of strain during the co-seismic phase (Figure 3g-I and Figure 4c). During the post-seismic phase, these strain gages (blue curves in Figure 3g-i, blue and red curves in Figure 4c), are subjected to a long-lasting strain decay. As observed on the macroscopic data, this phase is particularly well developed at high P_c. The duration of this phase increase from ~0.2 to ~3s increasing P_c from 30 to 90 MPa. The same behaviour for GM_f for the strain gages located far from the co-seismic strain drop (Figure 3j-l and Figure 4d). Similarly, post-seismic phase seems to emerge for M_{asp} at large confining pressure (blue curve in Figure 3f). This result demonstrates that the post-seismic phase, associated with afterslip is mostly observed far from the co-seismic strain drop areas (Figure S8), and well captured by local strain gauges measurements (Figure 3g-l, Figure 4c and d).

In summary, the macroscopic and strain gauge data show that the spatial and temporal evolution of slip and strain is more complex for heterogeneous faults than for homogeneous ones. In particular, the nucleation phase of heterogeneous faults is reduced in time and space compared to G_f. However, heterogeneities favour local stress/strain changes subsequently to the co-seismic phase (i.e., confined stress/strain drop), that give rise to a stress/strain deficit at the edge of the rupture. This stress/strain deficit favour the emergence of fault afterslip.

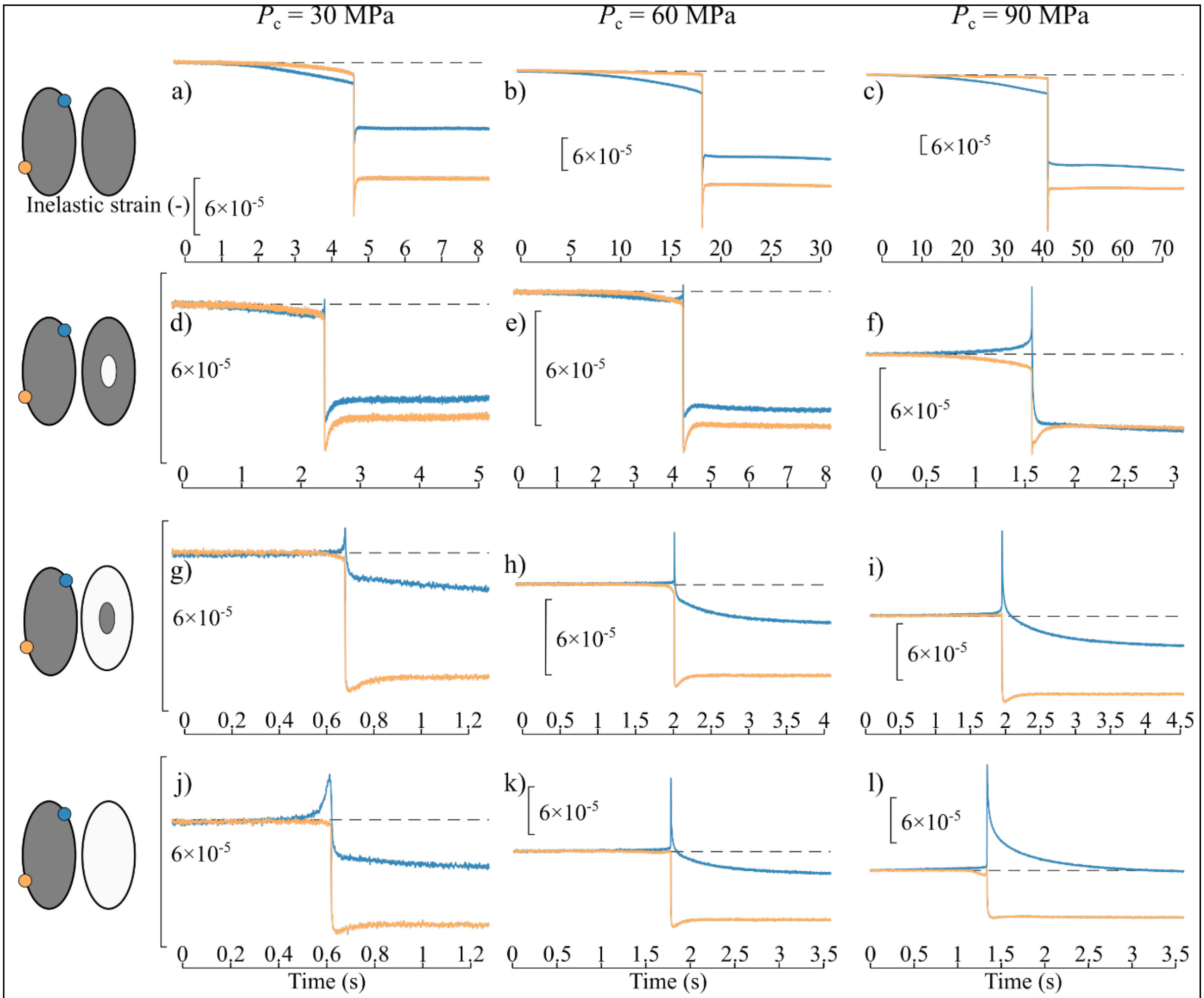

Figure 3: Inelastic strain measurement obtained from two strain gauges as a function of time for the tested fault composition. SG5 (orange), having often the larger co-seismic strain drop; and SG2 (blue) having often the largest post-seismic long-term strain drop. For each case, a typical seismic event is presented. The symbols of the left represent the two sides of the fault tested (grey for granite and white for marble). a-c) G_f, d-f) M_{asp}, g-i) G_{asp}, j-l) GM_f. a,d,g,j) P_c = 30 MPa, b,e,h,k) P_c = 60 MPa and c,f,i,l) P_c = 90 MPa. Note that the inelastic strain scale is different for each plot. The colour of the curve represents the strain gauge position on the sample schematic. See Figure 4 and Figure S7 in the supplementary material for the data measured at all the strain gauges.

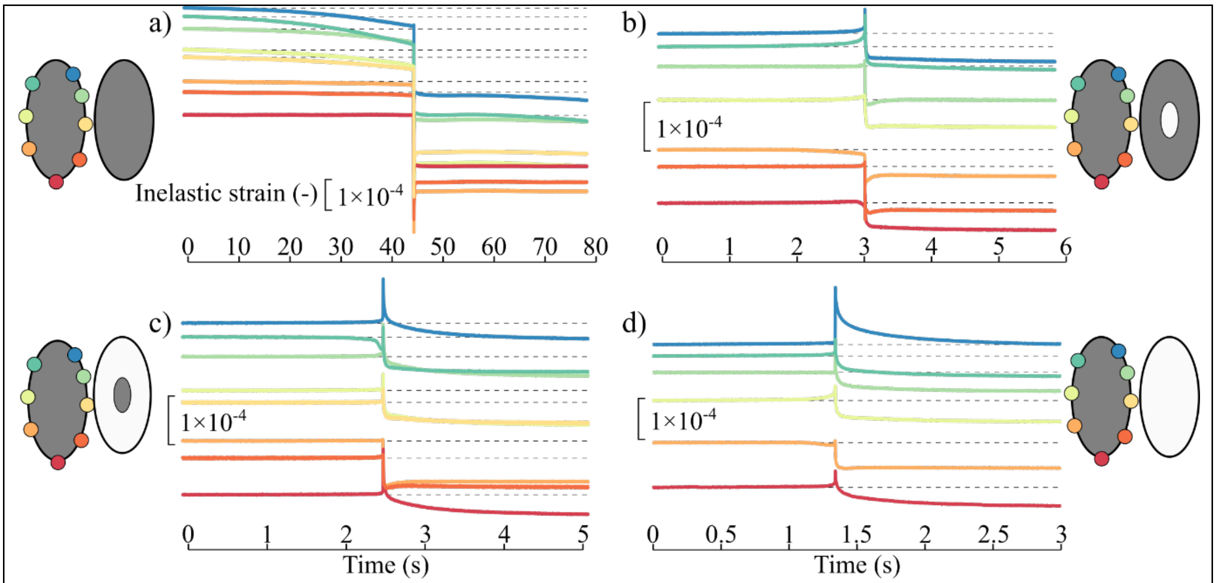

Figure 4: Inelastic strain measurement obtained from the eight strain gauges as a function of time for the tested fault composition at 90 MPa of confining pressure. For each case, a typical seismic event is presented. The symbols of the left represent the two sides of the fault tested (grey for granite and white for marble). a) G_f, b) M_{asp}, c) G_{asp}, d) GM_f. Note that the inelastic strain scale is different for each plot. The colour of the curve represents the strain gauge position on the sample schematic. See Figure S7 in the supplementary material for the data at all tested confining pressure.

4. Discussion

Our experiments highlight that frictional heterogeneities are able to modify the seismic cycle of a simple geometry fault. Particularly, granite-granite contacts favour the release of the accumulated stress through dynamic events. Instead, for the granite-marble contact, stress is released not only through dynamic events, but also through fault afterslip during a post-seismic phase. This behaviour is observed at all the tested confining pressures. However, higher confining pressures tend to favour fault afterslip of larger magnitude that last longer (Figure 2 and Figure 3). Our experiments are in this sense in agreement with rate-and-state models proposed for afterslip (Marone et al., 1991), as frictional heterogeneity are needed (or at least help) for the emergence of afterslip.

As stated previously, we find that fault afterslip is preferentially observed on strain gauges that exhibits little to no dynamic co-seismic strain drop (Figure S8). These results agree with observations from natural earthquake, where afterslip tends to occur in region devoid of co-seismic slip (Barbot et al., 2009; Gualandi et al., 2017; Hsu et al., 2002; Lu & Zhou, 2022; Miyazaki et al., 2004; Perfettini & Avouac, 2007) or with a little overlap (Barnhart et al., 2016; Hsu et al., 2006, 2009; Lin et al., 2013; Ozawa et al., 2012; Wimpenny et al., 2017).

Our experiments suggest that for afterslip to take place during our experiments, two mutually dependent conditions are required: (i) a seismic event confined within the experimental fault length, and (ii) a zone around the co-seismic rupture that is critically loaded and not prone to seismic behaviour, i.e., exhibiting preferentially aseismic slip or velocity strengthening behaviour. In our case, these conditions are favoured along the granite-marble contacts. Particularly, the case of G_{asp} sample demonstrates that frictional heterogeneities can be a key parameter for large afterslip (Figure 2, Figure 3g-I and Figure 4c).

However, the bi-material fault experiment (GM_f) is more puzzling. Even if the fault is composed of two materials, the frictional property of this bi-material interface should be constant across the fault, and should therefore produce seismic or aseismic slip. However, the behaviour is similar to G_{asp}, i.e., dynamic events are confined within the fault length, and fault afterslip occurs in areas devoid of co-seismic rupture (Figure 3j-l). A possible explanation could be that stress heterogeneity (Figure S9 and S10 in the supplementary material) induce highly localized spatial frictional changes of the interface, and a transition from velocity strengthening to velocity weakening behaviour along the fault due to plastic processes at the scale of asperities, as observed previously in calcite-rich bare surface (Aubry et al., 2020). The second hypothesis is the development of a patch of granite rich fault gouge along the interface, allowing to nucleate and propagate locally a dynamic instability (Figure S11 in the supplementary material).

To understand further the dynamics of fault afterslip, we analyse our post-seismic data within the rate-and-state framework. For that, we used the strain gauge measurements, in which the transition between co-seismic and post-seismic phase is clearly identified as it is separated in space and time (Figure 3 and Figure 4). To prevent possible contamination of afterslip motion by the co-seismic rupture, we assume that the fault afterslip begins at the end of the rapid strain drop recorded by the strain gauge located the closest to the dynamic rupture (Figure S13). We consider the end of the post-seismic phase when the inelastic strain rate at the strain gauges goes back visually to 0. In this rate-and-state framework, we assume that all the strain released during the post-seismic phase occurs on the frictional interface, and that nothing is released within the bulk of the sample, which is commonly assumed for natural events. Note that for the performed experiments, this assumption seems reasonable as no bulk deformations has been observed on the post-mortem analysis of M_f and G_{asp} samples. We model the slipping region as a spring-slider system obeying rate-and-state friction (Dieterich, 1979; Ruina, 1983). Assuming steady-state approximation and that the loading rate during this phase is negligible, the strain relaxation during post-seismic deformation on a frictional interface can be described as (Helmstetter & Shaw, 2009; Marone et al., 1991; Scholz, 2019):

$$\varepsilon = \dot{\varepsilon}_0 t_0 \ln\left(\frac{t}{t_0} + 1\right), \qquad (1)$$

$$\text{with } t_0 = \frac{\sigma_{\mathrm{n}}(a-b)^*}{(k/K)\dot{\varepsilon}_0} \qquad (2)$$

where σ_n is the normal stress acting on the fault, $(a\text{-}b)^*$ is the apparent steady-state rate-and-state parameter, k is the spring stiffness, K is a coefficient relating the change in axial strain with fault slip ($\varepsilon = K\delta$, δ being the slip), $\dot{\varepsilon}_0$ is the strain rate observed at the strain gauge location at the onset of afterslip, and t_0 is a characteristic time. The spring stiffness, k, relates the change in shear stress on the fault during the initial linear elastic loading of the sample, and is directly measured experimentally. The parameters K is estimated through finite elements analysis following the method developed by Dublanchet, (2024). This approach accounts for the geometry of the fault and of the sample (See supplementary material section 7 for details). K depends on the strain gauge location, e.g., K=14.5 m^{-1} for SG2.

For the inversions, we fixed $\dot{\varepsilon}_0$ using the value retrieved experimentally on the strain gauge used, at the onset of fault afterslip, and we only invert for t_0. Eq. (1) provides a good fit of our experimental data (Figure 5a and Figure S12), highlighting that the released strain related to fault afterslip evolves as a logarithmic function of time, as observed after natural earthquakes (e.g., Barbot et al., 2009; Cheloni et al., 2010; Smith & Wyss, 1968; Yagi et al., 2001). Note that using equation (1) and (2), only positive values of $(a\text{-}b)^*$ are considered, i.e., velocity strengthening behaviour. Other approximations exist involving negative values of $(a\text{-}b)^*$, i.e., velocity weakening behaviour, (Helmstetter & Shaw, 2009), however they imply stiffness or stress conditions ($k > k_c$, where k_c is a critical stiffness; or $\tau \ll \tau_{ss}$, where τ_{ss} is the shear stress at steady state; see Helmstetter & Shaw, 2009 Table 2) that are not realistic for our performed experiments.

Assuming this hypothesis, the inversions conducted imposing our measurement of $\dot{\varepsilon}_0$ demonstrate at first order that, an increase in $\dot{\varepsilon}_0$ leads to a decrease in t_0 (Figure 5b and 5c). Considering only the experiments conducted during the loading step, t_0 is slightly increasing with increasing confining pressure, for both G_{asp} and GM_f (Figure 5b). In addition, the inverted values are generally larger for GM_f than for G_{asp}, in agreement with the increase in final strain released by fault afterslip. For both samples, the inverted t_0 are of the order of few milliseconds, that is, ~3 orders of magnitude shorter than the total duration of post-seismic phase. Assuming simply Eq. (2), this increase in t_0 is expected to result from an increase in $(a\text{-}b)^*$ with increasing confining pressure, since the increase in normal stress acting on the fault at each confining pressure tested is not enough to explain the observed trend (Figure 5b). Interestingly, the trend is different for the experiments conducted during the unloading step of the experiments, i.e., decreasing the confining pressure from 90 MPa to 30 MPa (Figure 5c). Once the fault surface has experienced stick-slip events and fault afterslip at P_c = 90 MPa, the frictional properties of the fault seem to remain similar to the one observed at 90 MPa. For these experiments, the general trend in t_0 can be explained by Eq. (2), assuming simply the change in normal stress at the different confining pressure tested, and a similar value of $(a\text{-}b)^* = 0.006$ (Figure 5c).

Thanks to our direct experimental and numerical measurement of σ_n, k, K and $\dot{\varepsilon}_0$, $(a\text{-}b)^*$ can be estimated from Eq. (2) for each event. Note that these estimates are expected to represent the frictional parameters during the afterslip phase, and representative of the granite-marble interface only, since we conducted the inversions only for G_{asp} and GM_f. Assuming the values of t_0 inverted from our inversion and our direct measurements of $\dot{\varepsilon}_0$, an increase of $(a\text{-}b)^*$ is observed with increasing the final values of post-seismic strain (Figure 5d). In addition, our results demonstrate that increasing the confining pressure (i.e., the normal stress) leads to an increase in $(a\text{-}b)^*$ for both G_{asp} and GM_f (transparency datapoint in Figure 5d). This increase in $(a\text{-}b)^*$ could be directly related to an increase in $(a\text{-}b)$ (here rate-and-state parameters) of the marble-granite contact with increasing confining pressure. Indeed, the increase of $(a\text{-}b)^*$ with confining pressure is similar in magnitude than the increase in $(a\text{-}b)$ obtained for calcite gouge under the same normal stress conditions previously documented (Carpenter et al., 2016; Verberne et al., 2015). In agreement with the inverted values of t_0, GM_f presents generally larger values of $(a\text{-}b)^*$ and final post-seismic strain release (Figure 5d). However, the events recorded at 60 MPa and 30 MPa confining pressure during the unloading step of the experiments (i.e., after the experiments conducted at 90 MPa confining pressure), exhibit larger post-seismic strain, and larger values in $(a\text{-}b)^*$ than the events conducted at the same confining pressure during the loading step (Figure 5d). Therefore, after a fault interface has undergone stick-slip events and afterslip at P_c = 90 MPa, its frictional properties retain a memory of the past deformation. Similar observations have been previously made on gouge samples (Hong & Marone, 2005; Pozzi et al., 2022; Scuderi et al., 2017), suggesting that our inversions of the apparent rate-and-state parameters, through our measurements of post-seismic strain release, are a real proxy for the frictional parameters of the fault at the strain gauge location.

Remarkably, analysing all experiments together, the inverted $(a\text{-}b)^*$ align for each tested confining pressure (Figure 5d). At large confining pressure, similar values of post-seismic strain release requires smaller $(a\text{-}b)^*$ values than at low confining pressure. These results trend to demonstrate that the amplitude of the strain release due to fault afterslip is mostly controlled by $\sigma_n(a\text{-}b)^*$. Indeed, multiplying each values of $(a\text{-}b)^*$ by the normal stress σ_n applied on the fault at the onset of post-seismic phase, collapses all the data set (Figure 5e). Our results confirm that fitting the fault afterslip of real earthquakes can provide a good estimate of the local frictional parameters of the fault. However, since the normal stress (or effective normal stress) remains poorly constrain along natural faults, only the inversion of $\sigma_n(a\text{-}b)^*$ (as performed in some natural afterslip inversion studies, e.g., Lin et al., 2013; Perfettini et al., 2010; Perfettini & Avouac, 2004, 2007; Wimpenny et al., 2017) can provide an element of comparison between the different stations, or between different earthquakes.

Finally, our results also demonstrate that $\dot{\varepsilon}_0$ trend to increase with confining pressure (Figure 5b and c), and with the average stress drop during instabilities (Figure 5f). This increase in $\dot{\varepsilon}_0$ leads to the decrease in t_0 observed at each confining pressure, as expected by the theoretical predictions obtained from Eq. (2) (Figure 5b and c). This increase in $\dot{\varepsilon}_0$ with P_c can be attributed to an increase in sliding velocity during the confined co-seismic ruptures. Indeed, the strain rate depends on the slip velocity time the parameter K ($\dot{\varepsilon} = KV_s$). As K is constant in the tested range of normal stress, $\dot{\varepsilon}$ is a direct function of the slip velocity reached at the onset of the fault afterslip. Following previous studies, the slip velocity at the onset of fault afterslip is expected to be a function of the stress drop and of the normal stress following $V_0 = V_{\mathrm{pl}} \exp\left[\frac{\Delta\tau}{(a-b)\sigma_n}\right]$ (Perfettini & Ampuero, 2008; Perfettini & Avouac, 2007). Even if our measurement $\Delta\tau$ are obtained far from the fault (estimated from our pressure transducers), and therefore, potentially underestimated, our experimental results seem to confirm this exponential relationship between V_0 and $\Delta\tau$ (Figure 5f). However, the role of $\dot{\varepsilon}_0$ on the final value of strain release during the post-seismic slip remains secondary compared to $\sigma_n(a\text{-}b)^*$ that has a predominant effect (Figure 5e).

In summary, the evolution of the fault afterslip is well explained by the rate-and-state framework, and appears to be a combination of 1) the strain rate at the onset of afterslip $\dot{\varepsilon}_0$, which trend to decrease t_0 and 2) the frictional properties (i.e., $(a\text{-}b)^*$) around the area experiencing a dynamic stress/strain drop, which tends to increase with confining pressure.

For natural earthquakes, afterslip has been often proposed as the main driving force of the aftershock sequences (Avouac, 2015; Helmstetter & Shaw, 2009; and references therein). If the performed experiments do not allow to correlate afterslip and aftershock sequence (as no acoustic emission were emitted during afterslip sequences), they are able to identify the main parameters influencing the amplitude of afterslip. Our data alongside with recent experimental data performed on heterogeneous fault material (e.g., Arts et al., 2024; Bedford et al., 2022; Song & McLaskey, 2024) highlight the major role of frictional heterogeneity on the fault strength and stability. In particular, they allow for the emergence of afterslip similar to the one occurring after large earthquakes.

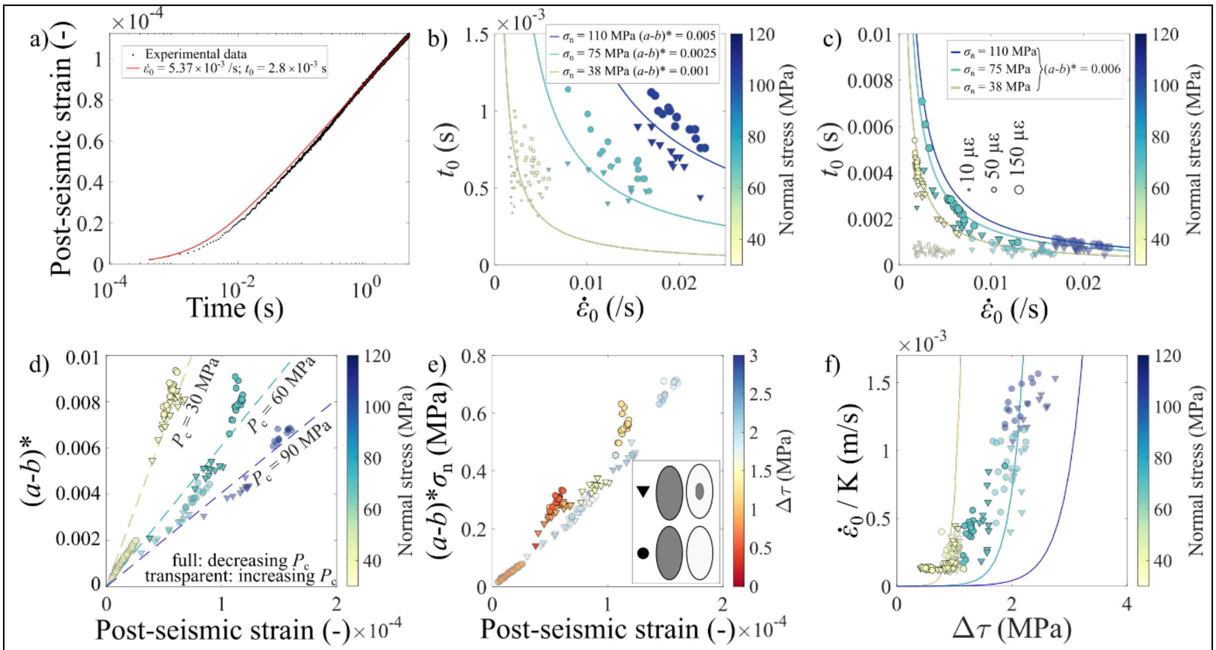

Figure 5: a) Post-seismic strain as a function of time measured experimentally at one strain gauge SG2, along with the modelled one using equation (1). Here, the experimental data are for the strain measured at strain gauge 2 of the GM_f at P_c = 60 MPa. The red curve is the best fit using the experimentally retrieved $\dot{\varepsilon}_0$ and inverted t_0. The blue curve is the best fit inverting both $\dot{\varepsilon}_0$ and t_0. b) Measured strain rate at the onset of post-seismic phase $\dot{\varepsilon}_0$ as a function of the inverted t_0 for all the afterslip recorded at strain gauge for the experiments conducted during the loading step (i.e., increasing confining pressure) of the experiments. The solid lines correspond to the estimate of t_0 as a function of $\dot{\varepsilon}_0$ for the three average values of σ_n and (*a*-*b*)*. c) Measured strain rate at the onset of post-seismic phase $\dot{\varepsilon}_0$ as a function of the inverted t_0 for all the afterslip recorded at strain gauge for the experiments conducted during the unloading step. The data presented in figure b) are displayed in transparency. For panel b) and c), the size of the datapoint represent the total amplitude of post-seismic strain. d) Apparent rate-and-state parameter $(a\text{-}b)^*$ obtained from the inverted t_0 and the measured $\dot{\varepsilon}_0$, k and σ_n (equation 2) as a function of the post-seismic strain. e) Same as panel d) except that (*a*-*b*)* is multiplied by the normal stress, allowing to collapse the data. The colour bar represents the macroscopic shear stress drop, $\Delta\tau$. f) Measured strain rate at the onset of post-seismic phase, as a function of the macroscopic shear stress drop, $\Delta\tau$. The full curves show $\frac{\dot{\varepsilon}_0}{K} = V_{pl} \exp\left[\frac{\Delta\tau}{(a-b)\sigma_n}\right]$, with V_{pl} being the far field loading rate (1.4 μm/s), (*a*-*b*) = 0.003, and for the three tested normal stress. For panels b-f) triangles and circles represent G_{asp} and GM_f, respectively. For panel c-f), the datapoint in transparency are the one obtained during the rising confining pressure step and the full datapoint are during the decreasing confining pressure step.

5. Conclusion

The experimental results presented in this manuscript challenge previous hypotheses derived from natural observations regarding the emergence of fault afterslip following large earthquakes. At the scale of our experiments, the presence of stress heterogeneities along the fault, which can potentially arrest seismic ruptures, does not appear sufficient to trigger a significant post-seismic phase. Instead, the emergence of afterslip in our experiments results from the interaction between a propagating seismic front, which stops in an aseismic region, causing a substantial increase in stress that is then released by fault afterslip. Our results are consistent with natural observations, including (i) afterslip occurring preferentially outside of the co-seismic rupture area, and (ii) a slip evolving with the logarithm of time. The measured afterslip in our experiments are explained by simple model involving velocity-weakening patches, governed by a rate-and-state friction law, surrounded by a velocity-strengthening interface. This is supported by (i) the imposed rheology of our experimental faults, and (ii) the observed exponential increase in initial afterslip velocity with increasing stress drop. Finally, our results indicate that the afterslip magnitude is likely controlled by both the frictional properties of velocity-strengthening patches and the normal stress acting along the fault plane. Due to this complexity, independently analysing these parameters from natural afterslip measurements is expected to remain challenging, especially given the uncertain on the stress conditions along natural faults.

Acknowledgment

This research has been founding by European Research Council (ERC) Starting Grant 101041966 (HOPE). The authors thanks Marie Violay for providing the sample and the sample preparation tools. The authors thanks Julien Ambre for the technical help in the laboratory. The authors thank Federica Paglialunga and Barnaby Fryer for the fruitful discussion.

References

Aben, F. M., & Brantut, N. (2023). Rupture and Afterslip Controlled by Spontaneous Local Fluid Flow in Crustal Rock. *Journal of Geophysical Research: Solid Earth*, *128*(11), e2023JB027534. https://doi.org/10.1029/2023JB027534

Arts, J. P. B., Niemeijer, R., Drury, M. R., Willingshofer, E., & Matenco, L. C. (2024). The frictional strength and stability of spatially heterogeneous fault gouges. *Earth and Planetary Science Letters*, *628*(118586). https://doi.org/10.1016/j.epsl.2024.118586

Aubry, J., Passelègue, F. X., Escartín, J., Gasc, J., Deldicque, D., & Schubnel, A. (2020). Fault Stability Across the Seismogenic Zone. *Journal of Geophysical Research: Solid Earth*, *125*(8), e2020JB019670. https://doi.org/10.1029/2020JB019670

Avouac, J. P. (2015). From geodetic imaging of seismic and aseismic fault slip to dynamic modeling of the seismic cycle. *Annual Review of Earth and Planetary Sciences*, *43*, 233–271. https://doi.org/10.1146/annurev-earth-060614-105302

Barbot, S., Fialko, Y., & Bock, Y. (2009). Postseismic deformation due to the Mw 6.0 2004 Parkfield earthquake: Stress-driven creep on a fault with spatially variable rate-and-state friction parameters. *Journal of Geophysical Research: Solid Earth*, *114*(B7). https://doi.org/10.1029/2008JB005748

Barnhart, W. D., Murray, J. R., Briggs, R. W., Gomez, F., Miles, C. P. J., Svarc, J., Riquelme, S., & Stressler, B. J. (2016). Coseismic slip and early afterslip of the 2015 Illapel, Chile, earthquake: Implications for frictional heterogeneity and coastal uplift. *Journal of Geophysical Research: Solid Earth*, *121*(8), 6172–6191. https://doi.org/10.1002/2016JB013124

Bedford, J. D., Faulkner, D. R., & Lapusta, N. (2022). Fault rock heterogeneity can produce fault weakness and reduce fault stability. *Nature Communications*, *13*(326). https://doi.org/10.1038/s41467-022-27998-2

Brantut, N., Schubnel, A., & Guéguen, Y. (2011). Damage and rupture dynamics at the brittle-ductile transition: The case of gypsum. *Journal of Geophysical Research: Solid Earth*, *116*(B1). https://doi.org/10.1029/2010JB007675

Caniven, Y., & Dominguez, S. (2021). Validation of a Multilayered Analog Model Integrating Crust-Mantle Visco-Elastic Coupling to Investigate Subduction Megathrust Earthquake Cycle. *Journal of Geophysical Research: Solid Earth*, *126*(2), e2020JB020342. https://doi.org/10.1029/2020JB020342

Caniven, Y., Dominguez, S., Soliva, R., Cattin, R., Peyret, M., Marchandon, M., Romano, C., & Strak, V. (2015). A new multilayered visco-elasto-plastic experimental model to study strike-slip fault seismic cycle. *Tectonics*, *34*(2), 232–264. https://doi.org/10.1002/2014TC003701

Carpenter, B. M., Collettini, C., Viti, C., & Cavallo, A. (2016). The influence of normal stress and sliding velocity on the frictional behaviour of calcite at room temperature: Insights from laboratory experiments and microstructural observations. *Geophysical Journal International*, *205*(1), 548–561. https://doi.org/10.1093/gji/ggw038

Cheloni, D., D'Agostino, N., D'Anastasio, E., Avallone, A., Mantenuto, S., Giuliani, R., Mattone, M., Calcaterra, S., Gambino, P., Dominici, D., Radicioni, F., & Fastellini, G. (2010). Coseismic and initial post-seismic slip of the 2009 Mw 6.3 L'Aquila earthquake, Italy, from GPS measurements. *Geophysical Journal International*, *181*(3), 1539–1546. https://doi.org/10.1111/j.1365-246X.2010.04584.x

Dieterich, J. H. (1978). Time-dependent friction and the mechanics of stick-slip. *Pure and Applied Geophysics*, *116*(4–5), 790–806. https://doi.org/10.1007/BF00876539

Dieterich, J. H. (1979). Modeling of rock friction 1. Experimental results and constitutive equations. *Journal of Geophysical Research: Solid Earth*, *84*(B5), 2161–2168. https://doi.org/10.1029/JB084iB05p02161

Fredrich, J. T., Evans, B., & Wong, T. (1989). Brittle to plastic transition in Carrara Marble. *Journal of Geophisical Research*, *94*(B4), 4129–4145. https://doi.org/10.1029/JB094iB04p04129

Fukuda, J., Johnson, K. M., Larson, K. M., & Miyazaki, S. (2009). Fault friction parameters inferred from the early stages of afterslip following the 2003 Tokachi-oki earthquake. *Journal of Geophysical Research: Solid Earth*, *114*(4). https://doi.org/10.1029/2008JB006166

Gualandi, A., Avouac, J. P., Galetzka, J., Genrich, J. F., Blewitt, G., Adhikari, L. B., Koirala, B. P., Gupta, R., Upreti, B. N., Pratt-Sitaula, B., & Liu-Zeng, J. (2017). Pre- and post-seismic deformation related to the 2015, Mw7.8 Gorkha earthquake, Nepal. *Tectonophysics*, *714–715*, 90–106. https://doi.org/10.1016/j.tecto.2016.06.014

Helmstetter, A., & Shaw, B. E. (2009). Afterslip and aftershocks in the rate-and-state friction law. *Journal of Geophysical Research: Solid Earth*, *114*(1). https://doi.org/10.1029/2007JB005077

Hirose, H., & Hirahara, K. (2004). A 3-D quasi-static model for a variety of slip behaviors on a subduction fault. *Pure and Applied Geophysics*, *161*, 2417–2431. https://doi.org/10.1007/s00024-004-2573-7

Hong, T., & Marone, C. (2005). Effects of normal stress perturbations on the frictional properties of simulated faults. *Geochemistry, Geophysics, Geosystems*, *6*(3). https://doi.org/10.1029/2004GC000821

Hsu, Y.-J., Bechor, N., Segall, P., Yu, S. B., Kuo, L. C., & Ma, K. F. (2002). Rapid afterslip following the 1999 Chi-Chi, Taiwan earthquake. *Geophysical Research Letters*, *29*(16), 1–4. https://doi.org/10.1029/2002GL014967

Hsu, Y.-J., Simons, M., Avouac, J.-P., Galetzka, J., Sieh, K., Chlieh, M., Natawidjaja, D., Prawirodirdjo, L., & Bock, Y. (2006). Frictional afterslip following the 2005 Nias-Simeulue earthquake, Sumatra. *Science*, *312*(5782), 1921–1926. https://doi.org/10.1126/science.1126960

Hsu, Y.-J., Yu, S. B., & Chen, H. Y. (2009). Coseismic and postseismic deformation associated with the 2003 Chengkung, Taiwan, earthquake. *Geophysical Journal International*, *176*(2), 420–430. https://doi.org/10.1111/j.1365-246X.2008.04009.x

Ke, C. Y., McLaskey, G. C., & Kammer, D. S. (2021). The earthquake arrest zone. *Geophysical Journal International*, *224*(1), 581–589. https://doi.org/10.1093/gji/ggaa386

Lin, Y. N. N., Sladen, A., Ortega-Culaciati, F., Simons, M., Avouac, J. P., Fielding, E. J., Brooks, B. A., Bevis, M., Genrich, J., Rietbrock, A., Vigny, C., Smalley, R., & Socquet, A. (2013). Coseismic and postseismic slip associated with the 2010 Maule Earthquake, Chile: Characterizing the Arauco Peninsula barrier effect. *Journal of Geophysical Research: Solid Earth*, *118*(6), 3142–3159. https://doi.org/10.1002/jgrb.50207

Lockner, D. A. (1998). A generalized law for brittle deformation of Westerly granite. *Journal of Geophysical Research: Solid Earth*, *103*(B3), 5107–5123. https://doi.org/10.1029/97JB03211

Lockner, D. A., Kilgore, B. D., Beeler, N. M., & Moore, D. E. (2017). The transition from frictional sliding to shear melting in laboratory stick-slip experiments. In *Fault zone dynamic processes: Evolution of fault properties during seismic rupture* (pp. 105–131).

Lu, L., & Zhou, Y. (2022). Co- and post-seismic slip analysis of the 2017 MW7.3 Sarpol Zahab earthquake using Sentinel-1 data. *Geodesy and Geodynamics*, *13*(2), 151–159. https://doi.org/10.1016/j.geog.2021.10.004

Marone, C. J., Scholtz, C. H., & Bilham, R. (1991). On the mechanics of earthquake afterslip. *Journal of Geophysical Research*, *96*(B5), 8441–8452. https://doi.org/10.1029/91JB00275

Meade, B. J. (2024). Kinematic Afterslip Patterns. *Geophysical Research Letters*, *51*(1). https://doi.org/10.1029/2023GL105797

Meyer, G. G., Brantut, N., Mitchell, T. M., & Meredith, P. G. (2019). Fault reactivation and strain partitioning across the brittle-ductile transition. *Geology*. https://doi.org/10.1130/G46516.1

Miyazaki, S., Segall, P., Fukuda, J., & Kato, T. (2004). Space time distribution of afterslip following the 2003 Tokachi-oki earthquake: Implications for variations in fault zone frictional properties. *Geophysical Research Letters*, *31*(6). https://doi.org/10.1029/2003gl019410

Ozawa, S., Nishimura, T., Munekane, H., Suito, H., Kobayashi, T., Tobita, M., & Imakiire, T. (2012). Preceding, coseismic, and postseismic slips of the 2011 Tohoku earthquake, Japan. *Journal of Geophysical Research: Solid Earth*, *117*(B7). https://doi.org/10.1029/2011JB009120

Passelègue, F. X., Almakari, M., Dublanchet, P., Barras, F., Fortin, J., & Violay, M. (2020). Initial effective stress controls the nature of earthquakes. *Nature Communications*, *11*(1), 1–8. https://doi.org/10.1038/s41467-020-18937-0

Passelègue, F. X., Schubnel, A., Nielsen, S., Bhat, H. S., Deldicque, D., & Madariaga, R. (2016). Dynamic rupture processes inferred from laboratory microearthquakes. *Journal of Geophysical Research: Solid Earth*, *121*(6), 4343–4365. https://doi.org/10.1002/2015JB012694

Perfettini, H., & Ampuero, J. P. (2008). Dynamics of a velocity strengthening fault region: Implications for slow earthquakes and postseismic slip. *Journal of Geophysical Research: Solid Earth*, *113*(B9). https://doi.org/10.1029/2007JB005398

Perfettini, H., & Avouac, J. -P. (2004). Postseismic relaxation driven by brittle creep: A possible mechanism to reconcile geodetic measurements and the decay rate of aftershocks, application to the Chi-Chi earthquake, Taiwan. *Journal of Geophysical Research: Solid Earth*, *109*(B2). https://doi.org/10.1029/2003JB002488

Perfettini, H., & Avouac, J. P. (2007). Modeling aftership and aftershocks following the 1992 Landers earthquake. *Journal of Geophysical Research: Solid Earth*, *112*(B7). https://doi.org/10.1029/2006JB004399

Perfettini, H., Avouac, J. P., Tavera, H., Kositsky, A., Nocquet, J. M., Bondoux, F., Chlieh, M., Sladen, A., Audin, L., Farber, D. L., & Soler, P. (2010). Seismic and aseismic slip on the Central Peru megathrust. *Nature*, *465*(3894), 78–81. https://doi.org/10.1038/nature09062

Pozzi, G., Scuderi, M. M., Tinti, E., Nazzari, M., & Collettini, C. (2022). The Role of Fault Rock Fabric in the Dynamics of Laboratory Faults. *Journal of Geophysical Research: Solid Earth*, *127*(6). https://doi.org/10.1029/2021JB023779

Rice, J. R., & Gu, J. cheng. (1983). Earthquake aftereffects and triggered seismic phenomena. *Pure and Applied Geophysics*, *121*(2), 187–219. https://doi.org/10.1007/BF02590135

Ruina, A. (1983). Slip instability and state variable friction law. *Journal of Geophysical Research*, *88*, 10359–10370. https://doi.org/10.1029/JB088iB12p10359

Schmid, S. M., Paterson, M. S., & Boland, J. N. (1980). High temperature flow and dynamic recrystallization in carrara marble. *Tectonophysics*, *65*(3–4), 245–280. https://doi.org/10.1016/0040-1951(80)90077-3

Scholz, C. H. (2019). The Mechanics of Earthquakes and Faulting. In *The Mechanics of Earthquakes and Faulting* (3rd editio). Cambridge University Press. https://doi.org/10.1017/9781316681473

Scuderi, M. M., Collettini, C., Viti, C., Tinti, E., & Marone, C. (2017). Evolution of shear fabric in granular fault gouge from stable sliding to stick slip and implications for fault slip mode.

Geology, *45*(8), 731–734. https://doi.org/10.1130/G39033.1

Smith, S. W., & Wyss, M. (1968). Displacement on the San Andreas fault subsequent to the 1966 Parkfield earthquake. *Bulletin of the Seismological Society of America*, *58*(6), 1955–1973. https://doi.org/10.1785/BSSA0580061955

Song, J. Y., & McLaskey, G. C. (2024). Laboratory Earthquake Ruptures Contained by Velocity Strengthening Fault Patches. *Journal of Geophysical Research: Solid Earth*, *129*(4), 1–16. https://doi.org/10.1029/2023JB028509

Thompson, B. D., Young, R. P., & Lockner, D. A. (2009). Premonitory acoustic emissions and stick-slip in natural and smooth-faulted Westerly granite. *Journal of Geophysical Research: Solid Earth*, *114*(B2). https://doi.org/10.1029/2008JB005753

Tullis, J., & Yund, R. A. (1977). Experimental deformation of dry westerly granite. *Journal of Geophysical Research*, *82*(36), 5705–5718. https://doi.org/10.1029/JB082i036p05705

Verberne, B. A., Niemeijer, A. R., Bresser, J. H. P. De, & Spiers, C. J. (2015). Mechanical behavior and microstructure of simulated calcite fault gouge sheared at 20–600°C: Implications for natural faults in limestones. *Journal of Geophysical Research: Solid Earth*, *120*(12), 8169–8196. https://doi.org/10.1002/2015JB012292

Verberne, B. A., Spiers, C. J., Niemeijer, A. R., De Bresser, J. H. P., De Winter, D. A. M., & Plümper, O. (2014). Frictional Properties and Microstructure of Calcite-Rich Fault Gouges Sheared at Sub-Seismic Sliding Velocities. *Pure and Applied Geophysics*, *171*(10), 2617–2640. https://doi.org/10.1007/s00024-013-0760-0

Wimpenny, S., Copley, A., & Ingleby, T. (2017). Fault mechanics and post-seismic deformation at Bam, SE Iran. *Geophysical Journal International*, *209*(2), 1018–1035. https://doi.org/10.1093/gji/ggx065

Wong, T. F. (1982). Micromechanics of faulting in westerly granite. *International Journal of Rock Mechanics and Mining Sciences And*, *19*(2), 49–64. https://doi.org/10.1016/0148-9062(82)91631-X

Yagi, Y., Kikuchi, M., & Nishimura, T. (2003). Co-seismic slip, post-seismic slip, and largest aftershock associated with the 1994 Sanriku-haruka-oki, Japan, earthquake. *Geophysical Research Letters*, *30*(22). https://doi.org/10.1029/2003GL018189

Yagi, Y., Kikuchi, M., & Sagiya, T. (2001). Co-seismic slip, post-seismic slip, and aftershocks associated with two large earthquakes in 1996 in Hyuga-nada, Japan. *Earth, Planets and Space*, *53*(8), 793–803. https://doi.org/10.1186/BF03351677